Efficient vibrational excitation of molecular nitrogen in low-pressure plasma with ultralow electron temperature

Masahiro Yamazaki and Koichi Sasaki

Division of Applied Quantum Science and Engineering, Hokkaido University, Kita 13, Nishi 8, Kita-ku, Sapporo 060-8628, Japan

E-mail: sasaki@qe.eng.hokudai.ac.jp

Abstract. We investigated the vibrational temperature of molecular nitrogen in the downstream of helicon-wave excited helium and argon-based plasmas. It was confirmed by optical emission spectroscopy that the major part of the helium plasma was at a recombining state and it had an ultralow electron temperature of approximately 0.1 eV. In spite of the ultralow electron temperature, the vibrational temperature of molecular nitrogen, which was added into the helium plasma, was higher than that in the argon-based plasma at an ionizing state with an electron temperature of 1.7 eV. According to the relationship between the rate coefficient of electron impact vibrational excitation and the electron temperature, the higher vibrational temperature in the helium plasma is not attributable to the more efficient vibrational excitation. Therefore, the higher vibrational temperature is owing to the less efficient destruction of vibrational excited states in the helium plasma with the ultralow electron temperature.

1. Introduction

The plasma-assisted catalytic synthesis of ammonia has a potential as a reservoir and a carrier of electric power delivered from distributed power sources such as windfarms and solar cells. The potential of the ammonia synthesis is related with the fact that the conventional Haber–Bosch process needs plant-level equipment and is not suitable to the distributed systems. In general, the first and rate-limiting step for the catalytic synthesis of ammonia is believed to be adsorption of nitric species on the catalyst surface. It has been considered that atomic nitrogen, which is produced in plasma by electron impact dissociation of molecular nitrogen, is the principal species for the adsorption in the plasma-assisted catalytic synthesis [1–3].

Molecular nitrogen has a dissociation energy of 9.7 eV [4]. Because of the high dissociation energy, the production of atomic nitrogen by electron impact dissociation of molecular nitrogen is inefficient even in plasmas with electron temperatures of 3-4 eV, since only a fraction ($\sim$ 10%) of electrons has kinetic energies exceeding the dissociation energy. Some researchers point out the usefulness of dissociative recombination of N_2^+ ($N_2^+ + e \rightarrow N + N$) [5–8]. However, this process has a large rate coefficient at an

electron temperature less than 1 eV [9–11], indicating that ordinary ionizing plasmas cannot utilize this process for the production of atomic nitrogen.

Recently, vibrational excited states of molecules at the electronic ground states attract much attention. It is believed that dissociation via vibrational excited states improves the efficiency of CO_2 splitting using plasmas [12–16]. In addition, it is pointed out that vibrational exited states can work as another species which have high adsorption probabilities on catalyst surfaces. The enhanced adsorption probability is believed to be obtained by the consumption of the vibrational energy for overcoming the activation energy of chemisorption. The enhanced chemisorption has been already reported in CH_4-Ni(100) [17], D_2-Cu(111) [18], N_2-noble metals [19–21], and CO_2-Cu systems [22]. If vibrational excited states of molecular nitrogen work effectively for the enhancement of the chemisorption probability, they may improve the energy efficiency of plasma-assisted catalytic synthesis of ammonia, since electrons with low kinetic energies can participate in the vibrational excitation.

The production and loss processes of radicals and atomic species in plasmas have been investigated rather intensively in the history of the reactive plasma research. This is because the interaction between radicals and solid-state surfaces has direct applications in the processing of thin films such as etching and deposition. In contrast, the investigation of the kinetics of vibrational excited states is remarkably insufficient in comparison with radicals. This may be partly because the gas reforming reactions mentioned above are the first realistic applications of vibrational excited states. However, thanks to the expectation for the reaction processes driven by vibrationally excited molecules, recently, experimental investigations on the fundamental aspects of vibrational kinetics in plasmas have made great progress with the help of sophisticated diagnostics [23–30].

The objective of the present work is to give an understanding on the kinetics of vibrational excited states (or the vibrational temperature) of molecular nitrogen. In particular, we focus on the importance of the electron temperature. Several authors have reported both the electron (or excitation) temperature and the vibrational temperature in plasmas at low [31], medium [32], and atmospheric pressures [33]. We can find the positive correlations between the electron and vibrational temperatures in their papers, where the electron temperatures are higher than 0.5 eV and the plasmas are at ionizing states. In this work, we employed a helicon-wave plasma source to produce helium and argon-based plasmas. The major part of the helium plasma was at a recombining state with an electron temperature of approximately 0.1 eV, whereas the argon-based plasma was at an ordinary ionizing state. The rate coefficient of the electronic excitation is negligibly small and the vibrational excitation is only the excitation process in the helium plasma, whereas both the electronic and vibrational excitations are possible in the ionizing argon-based plasma. By comparing the results obtained using the two plasmas, we have shown the importance of the ultralow electron temperature to realize a high vibrational temperature of molecular nitrogen.

2. Experiment

2.1. Plasma source

Figure 1 shows the helicon-wave plasma source we used in this work [34]. It was possible to generate a high-density plasma by applying an rf power of 3kW at 13.56 MHz to a helical antenna wound around a quartz tube with an inner diameter of 16 mm. The quartz tube was attached to a stainless-steel chamber, and the plasma produced in the quartz tube was transported to the downstream area. The discharge gas was pure helium or argon with the small addition (5%) of helium. The discharge gas was introduced into the upstream side of the plasma source. The pressure and the flow rate of helium in the helium discharge were 180 mTorr and 200 sccm, respectively, whereas they were 200 mTorr and 200 sccm in the argon-based discharge. The pressure of the argon-based gas was adjusted by reducing the evacuation speed using a gate valve. The plasma source had a uniform magnetic field of 550 G along the cylindrical axis.

The background of the present work was the synthesis of ammonia from the mixture of N_2 and H_2. The mixture of N_2 and H_2 was introduced into the downstream side of the stainless-steel chamber. To avoid the backward flows of N_2 and H_2 toward the upstream plasma, the stainless-steel chamber was divided into the upstream and downstream sides by placing an orifice with a diameter of 16 mm. The pressures of helium and the argon-based gas in the downstream side were 135 and 105 mTorr, respectively. The larger difference between the pressures of the argon-based gas in the upstream and downstream sides was due to the higher pumping speed of argon than helium. The lower pressure of the argon-based gas was necessary for the similar transports of the helium and argon-based plasmas to the downstream side. The nozzle for introducing the mixture of N_2 and H_2 was located at an axial distance of 5 cm from the orifice and at a radial distance of 15 cm from the cylindrical axis. The downstream side of the chamber was connected to a turbomolecular pump with a pumping speed of 1000 L/s. The negligible backward flows were confirmed by observing negligible optical emission intensities of molecular nitrogen and atomic hydrogen in the upstream side. The flow rates of both N_2 and H_2 were 20 sccm, which corresponded to the partial pressures of 3.0 and 2.6 mTorr, respectively, in the helium plasma, whereas they were both 0.5 mTorr in the argon-based plasma. The different partial pressures of N_2 and H_2 were caused by the different pumping speeds in the helium and argon-based plasmas. The partial pressures were determined using a quadrupole mass spectrometer (QMS) attached at port (B) in Fig. 1. We installed QMS in another vacuum chamber, and the QMS chamber was connected to the plasma chamber via an orifice with a diameter of 0.5 mm. The QMS chamber was differentially evacuated using another turbomolecular pump. The purpose for adding helium into argon was to calibrate the sensitivity of QMS. The measurements of various plasma parameters were carried out basically at the position where the mixture of N_2 and H_2 was introduced (port (A) in Fig, 1).

2.2. Laser Thomson scattering

We measured the electron density and the electron temperature of the helium plasma on the cylindrical axis by laser Thomson scattering. We injected the second harmonics (532 nm) of a Nd:YAG laser beam along the cylindrical axis via port (C) in Fig. 1. The laser energy was 150 mJ/pulse. The laser beam was focused using a lens, and the focal point was positioned at port (A). The scattered laser light which passed through port (A) was focused onto an optical fiber, and the optical fiber guided the scattered laser light to a triple-grating spectrograph (TGS) [35]. The stray laser light, whose wavelength was not shifted from the incident laser wavelength, was eliminated by the Rayleigh block in TGS. The scattered laser light transmitted through TGS was detected using a charge-coupled device camera with a gated image intensifier (ICCD camera). The scattered laser light was accumulated on the ICCD camera for 4000 laser shots. The spectrum of the scattered laser light was approximated by a Gaussian function, and the electron temperature and the electron density were evaluated from the width and the amplitude of the Gaussian function, respectively [36]. The amplitude of the scattered laser light was calibrated by the intensity of the rotational Raman scattering of molecular nitrogen at a known pressure.

2.3. Langmuir probe

Since the intensity of the laser Thomson scattering in the argon-based plasma was weaker than the detection limit, we estimated the electron density of the argon-based plasma using a Langmuir probe. The Langmuir probe was inserted from port (A), and we measured the ion saturation currents both in the helium and argon-based plasmas [37,38]. The probe tip was biased at -30 V with respect to the ground potential (the potential of the stainless-steel chamber). The electron density in the argon-based plasma was obtained from the ratio of the ion saturation currents in the helium and argon-based plasmas and the electron density in the helium plasma which was measured by laser Thomson scattering.

2.4. Optical emission spectroscopy

Optical emission spectroscopy was used for measuring the absolute densities of the electronic excited states of molecular nitrogen (the $B^3\Pi_g$ and $C^3\Pi_u$ states) and helium (the p^3D states with p being the principal quantum number). The transitions we observed were the first ($B^3\Pi_g$-$A^3\Sigma_u^+$) and second ($C^3\Pi_u$-$B^3\Pi_g$) positive systems of molecular nitrogen and $2^3P^o - p^3D$ of helium. The sensitivity of the spectroscopic system, which was composed of an optical window, a lens, an optical fiber, a Czerny-Turner spectrograph, and an ICCD camera, was calibrated using a tungsten standard lamp and a deuterium standard lamp to obtain the absolute emission coefficients (the numbers of photons emitted per unit volume and unit time) [12]. The absolute emission

coefficient was obtained by

$$\varepsilon = \frac{4\pi}{h\nu D}\frac{S_{\rm P}}{S_{\rm L}}\frac{G_{\rm L}}{G_{\rm P}}\frac{\Delta T_{\rm L}}{\Delta T_{\rm P}} I_{\rm L}\Delta\lambda_{\rm L}, \tag{1}$$

where $S_{\rm P}$ and $S_{\rm L}$ are the signals from the spectrograph when detecting the optical emissions from the plasma and the standard lamp, respectively, $I_{\rm L}$ is the spectral radiance of the lamp emission which is given in the unit of $\mathrm{Wm^{-3}sr^{-1}}$, $h\nu$ is the photon energy, D is the diameter of the plasma column, $\Delta\lambda_{\rm L}$ is the resolution of the spectrograph when measuring $S_{\rm L}$, $G_{\rm P}$ and $G_{\rm L}$ are the gains of the ICCD camera when measuring $S_{\rm P}$ and $S_{\rm L}$, respectively, and $\Delta T_{\rm P}$ and $\Delta T_{\rm L}$ are the gate widths when measuring $S_{\rm P}$ and $S_{\rm L}$, respectively. The absolute densities of $\mathrm{N_2(B^3\Pi_g)}$, $\mathrm{N_2(C^3\Pi_u)}$, and $\mathrm{He}(p^3\mathrm{D})$ were obtained from the emission coefficients and the transition probabilities [39]. The absolute densities of the p^3D states of helium were utilized to estimate the electron density and the electron temperature of the helium plasma at the recombining state. The detailed method for estimating the electron density and the electron temperature from the densities of $\mathrm{He}(p^3\mathrm{D})$ has been described in a previous paper [12]. The measurements of the $\mathrm{N_2(B^3\Pi_g)}$ and $\mathrm{N_2(C^3\Pi_u)}$ densities were carried out at port (A). On the other hand, we measured the He (p^3D) density in the upstream side just above the orifice, since the optical emission spectrum of the $2^3\mathrm{P^o}-p^3\mathrm{D}$ transition was contaminated significantly by molecular band spectra when we observed it at port (A).

2.5. Threshold ionization mass spectrometry

We employed threshold ionization mass spectrometry for measuring the density of atomic nitrogen and the vibrational temperatures of molecular nitrogen. The QMS chamber was positioned at port (A) and the sampling orifice was inserted into the plasma column when measuring the N density and the vibrational temperature. The electron beam energy of the QMS filament was varied between 10 and 50 eV. Since the threshold electron energies for $\mathrm{N + e \rightarrow N^+ + 2e}$ and $\mathrm{N_2 + e \rightarrow N^+ + N + 2e}$ are 15.6 and 24.3 eV, respectively, the QMS signal at $m/z = 14$ comes only from the former reaction if the electron energy is adjusted between the two threshold energies [40]. The absolute density of atomic nitrogen was obtained from the ratio of the QMS signals and the cross sections of the two ionization processes. On the other hand, we estimated the vibrational temperature of molecular nitrogen from the threshold ionization curve (the relationship between the QMS signal and the electron energy) at $m/z = 28$. The principle of the estimation of the vibrational temperature is the shift of the threshold ionization curve due to the vibrational excitation. The details of the threshold ionization mass spectrometry for estimating the vibrational temperature have been reported in a separate paper [41]. We believe that the sampling and transport processes in the QMS measurement did not affect the vibrational temperature, since a collisionless condition was realized in the QMS chamber with the differential pumping and the surface deactivation coefficient of $\mathrm{N_2}(\mathrm{X}^1\Sigma_g^+, v)$ is rather small ($< 10^{-3}$) [42].

2.6. Laser absorption spectroscopy

Laser absorption spectroscopy was used for measuring the translational temperatures of the metastable states of helium (2^3S_1) and argon ($4s^2[3/2]^o_2$)). The light sources were diode lasers. The transition lines for detecting He(2^3S_1) and Ar($4s^2[3/2]^o_2$) were $2^3S_1-2^3P^o_0$ (1082.909 nm) and $4s^2[3/2]^o_2-4p^2[3/2]_2$ (763.511 nm), respectively. The laser beams were injected into the plasmas through port (A), and the transmitted laser beams were detected using a photodiode. The polarizations of the laser beams were parallel to the magnetic field (the π polarization). The absorption spectra were obtained by scanning the laser wavelengths around the line center wavelengths. The Zeeman splitting in the magnetic field of 550 G made the absorption spectra complicated, but we obtained the densities of the metastable states from the wavelength-integrated absorption with the help of the knowledge on the transition probabilities [43]. The temperatures of He(2^3S_1) and Ar($4s^2[3/2]^o_2$) were estimated by fitting the absorption spectra with the superpositions of Zeeman-split lines with Doppler broadening. We assumed that the temperatures of He(2^3S_1) and Ar($4s^2[3/2]^o_2$) represented the gas temperatures of the helium and argon-based plasmas, respectively.

3. Results

3.1. Electron density and electron temperature

Figure 2 shows the spectrum of laser Thomson scattering observed in the helium plasma. The intensity of rotational Raman scattering of molecular nitrogen was negligible in comparison with Thomson scattering because of the low N_2 partial pressure (0.5-3 mTorr). Although the hatched wavelength region ($\Delta\lambda \leq 0.55$ nm) was masked by the Rayleigh block in TGS, we detected the light intensity in the masked region due to the huge stray light. The signal-to-noise ratio in the unmasked region is quite low, but we fitted the spectrum by a Gaussian function, as shown in Fig. 2. We employed the data at $0.55 \leq \lambda \leq 2.5$ nm for the fitting since the signal-to-noise ratio at $\lambda > 2.5$ nm was too low. According to the width of the Gaussian function, we evaluated $T_e = 1.6 \pm 0.2$ eV for the electron temperature. The electron density was evaluated from the amplitude of the Gaussian function, and it was $n_e = (6.0 \pm 0.6) \times 10^{18}$ m^{-3}. Note that these values were the electron temperature and the electron density on the cylindrical axis.

Figure 3(a) shows the optical emission spectrum of the helium plasma, where the vertical axis is given by the absolute emission coefficient. We assumed 10 cm for the line-of-sight for deducing the emission coefficient from the optical emission intensity. As indicated in the figure, the emission lines were assigned to the $2^3P^o-p^3D$, $2^3P^o-p^3S$ and $2^1S-p^1P^o$ transitions of helium [44,45]. We detected the optical emission lines from Rydberg states with $p \leq 16$. Since it is impossible to observe the optical emissions from the Rydberg states in an ionizing plasma [46, 47], the optical emission spectrum shown in Fig. 3(a) indicates that the helium plasma is at the recombining state and the Rydberg states are produced by three-body recombination $He^+ + e + e \rightarrow He^* + e$.

The population densities of electronic excited states of helium are plotted in Fig. 3(b) as a function of the ionization potential. As has been described in our previous papers [12, 46], the collisional-radiative model tells us that the population distribution of Rydberg states is approximated by the Saha-Boltzmann equation when the plasma is at the recombining state [44, 45]. The Saha-Boltzmann fitting is possible for the population distribution at $9 \leq p \leq 14$ in the data shown in Fig. 3(b), and the electron temperature and the electron density were evaluated from the slope and the intercept to be $T_\mathrm{e} = 0.10 \pm 0.02$ eV and $n_\mathrm{e} = (6.0 \pm 0.6) \times 10^{18}$ m^{-3}, respectively. The electron density evaluated by the Saha-Boltzmann fitting agreed with that measured by laser Thomson scattering. However, we found the significant difference between the electron temperatures measured by laser Thomson scattering and the Saha-Boltzmann fitting.

The discrepancy between the electron temperatures measured by laser Thomson scattering and the Saha-Boltzmann fitting was attributed to the difference in the observation position. A photograph of the helium plasma is shown in Fig. 4(a), which was taken using a consumer-grade digital camera from the radial direction when N_2 and H_2 were not introduced into the downstream-side chamber. As shown in the figure, the helium plasma had a radial structure. The color of the plasma in the central region was orange. The same orange plasma was observed in the quartz tube, indicating that the plasma in the central region was at the ionizing state. On the other hand, the color of the plasma in the outside region was pink, as shown in Fig. 4(a). It is noted here that the optical emission spectrum shown in Fig. 3(a) was obtained by the line-of-sight measurement along the radial direction. Therefore, it is understood that the electron temperature of $T_\mathrm{e} = 1.6$ eV, which was measured by laser Thomson scattering, represented the value in the central region, and $T_\mathrm{e} = 0.1$ eV, which was evaluated by the optical emission spectroscopy, represented the value in the outside region. Note that the volume of the outside region is eight times greater than that of the central region. Hence, the major part of the helium plasma had an ultralow electron temperature of approximately 0.1 eV.

The electron density in the argon-based plasma was estimated to be $n_\mathrm{e} = (8.0 \pm 0.8) \times 10^{17}$ m^{-3} by referring to the ion saturation current of the Langmuir probe and the electron density of the helium plasma. The electron temperature in the argon-based plasma at the position of port (A) was unknown, since the Thomson scattering signal was below the detection limit and the relationship between the voltage and the current of the Langmuir probe was distorted by the magnetic field and the fluctuation at the frequency of the rf power [37,38]. However, it was possible to detected the Thomson scattering signal in the upstream side just above the orifice. The electron temperature evaluated from the Thomson scattering spectrum was $T_\mathrm{e} = 1.7 \pm 0.2$ eV. Therefore, we speculated that the electron temperature of the argon-based plasma at the position of port (A) was similar to the electron temperature in the central part of the helium plasma. As shown in Fig. 4(b), we observed no anomalous radial transport of the argon-based plasma. By considering the electron density of $n_\mathrm{e} = 8 \times 10^{17}$ m^{-3} and by referring to the general knowledge that the recombining states are rarely observed in

argon plasmas [48, 49], it was estimated that the entire part of the argon-based plasma was at the ionizing state.

3.2. Densities of electronic excited states of molecular nitrogen

The optical emission spectra of the helium and argon-based plasmas with the addition of the mixture of N_2 and H_2 are shown in Fig. 5. The spectrum shown in Fig. 5(a) is almost occupied by the second positive system of molecular nitrogen, and in addition to it, the optical emission of the first negative system of N_2^+ is observed at 388.4 nm. The assignments on the vibrational quantum numbers are indicated in the figure. On the other hand, the spectrum shown in Fig. 5(b) is dominated by the first positive system of molecular nitrogen except the line emissions of atomic hydrogen and helium. The vibrational temperatures of $N_2(C^3\Pi_u)$ evaluated from the Boltzmann plots of Fig. 5(a) were 0.9 and 0.5 eV in the helium and argon-based plasmas, respectively, and the vibrational temperatures of $N_2(B^3\Pi_g)$ which were deduced from Fig. 5(b) were 0.6 eV in both the helium and argon-based plasmas. It is important to note that the optical emission intensity (the emission coefficient) was much higher in the helium plasma than the argon-based plasma. The densities of $N_2(B^3\Pi_g)$ and $N_2(C^3\Pi_u)$, which were evaluated from the emission coefficients and the transition probabilities [39], were $(5.0 \pm 0.1) \times 10^{14}$ and $(1.0 \pm 0.1) \times 10^{13}$ m^{-3} in the helium plasma, respectively, while they were $(7 \pm 2) \times 10^{12}$ and $(1.0 \pm 0.1) \times 10^{11}$ m^{-3} in the argon-based plasma.

3.3. Vibrational temperature of molecular nitrogen

The threshold ionization curves at $m/z = 28$, which were observed in the helium and argon-based plasmas, are shown in Fig. 6. The black curves show the threshold ionization curves which were observed without producing the plasmas. When the same measurements were carried out in the plasmas, we observed the shifts of the threshold ionization curves toward the low energy side, as shown in Fig. 6. Although we observed the decreases in the amplitudes of the threshold ionization curves by producing the plasmas, the amplitudes are normalized in Fig. 6 at the electron energy of 50 eV. We constructed a model for estimating the vibrational temperature of molecular nitrogen from the shifted threshold ionization curve. The details of the model has been described in a separate paper [41]. Briefly, we assumed that the vibrational excited states have the same cross section of electron impact ionization as the vibrational ground state except the shift of the threshold energy. The magnitudes of the shift were assumed to be equal to the vibrational energies. We assumed a Boltzmann distribution at a vibrational temperature T_v, and we calculated the threshold ionization curve which was expected at the vibrational temperature. By fitting the experimental threshold ionization curve with the calculated one, we estimated the vibrational temperature. The vibrational temperatures estimated from the threshold ionization curves shown in Figs. 6(a) and 6(b) were 0.34 ± 0.04 and 0.18 ± 0.04 eV for the helium and argon-based plasmas, respectively. These values are the vibrational temperatures of the electronic ground

state. Although vibrational temperatures of the ground state are lower than those of $N_2(B^3\Pi_g)$ and $N_2(C^3\Pi_u)$, we believe that the vibrational temperatures of the ground state are more relevant to reaction processes.

3.4. Density of atomic nitrogen

The green curve shown in Fig. 7 is the threshold ionization curve at $m/z = 14$, which was observed in the helium plasma. The appearance of the QMS signal was observed at an electron energy of approximately 15 eV, which agreed with the threshold of $N + e \rightarrow N^+ + 2e$. The blue curve shown in Fig. 7 was observed without producing the plasma. The amplitude of the blue curve in Fig. 7 is reduced by a factor which corresponds to the decrease in the molecular nitrogen density by the plasma production. The reduction factor was obtained from the decrease in the QMS signal at an electron energy of 50 eV and $m/z = 28$. The appearance energy of the blue curve (24.5 eV) agreed with the threshold energy of $N_2 + e \rightarrow N^+ + N + 2e$. Hence, it was judged that the QMS current observed at electron energies between 15 and 25 eV came from atomic nitrogen. The density of atomic nitrogen which was estimated from the QMS signal and the cross sections of the two ionization processes was $(2.0 \pm 0.2) \times 10^{19}$ m^{-3} in the helium plasma. On the other hand, the threshold ionization curve observed in the argon-based plasma was different from Fig. 7, and the QMS signal at electron energies between 15 and 25 eV was negligible. This means a low density of atomic nitrogen. Considering the detection limit of the QMS signal, we concluded that the density of atomic nitrogen in the argon-based plasma was lower than 2×10^{18} m^{-3}.

3.5. Gas temperature

When N_2 and H_2 were introduced to the downstream-side chamber at the flow rates of 20 sccm, we observed no absorption of the diode laser lights at the wavelengths for detecting $He(2^3S_1)$ and $Ar(4s^2[3/2]^o_2)$ in both the helium and argon-based plasmas. The absorptions corresponding to the detection-limit $He(2^3S_1)$ and $Ar(4s^2[3/2]^o_2)$ densities (1.2×10^{17} and 3×10^{15} m^{-3}, respectively) were observed at flow rates of 3 and 0.8 sccm in the helium and argon-based plasmas, respectively. Therefore, it was estimated that the $He(2^3S_1)$ and $Ar(4s^2[3/2]^o_2)$ densities at the flow rate of 20 sccm were much lower than the detection-limit densities. On the other hand, the temperatures deduced from the Doppler broadening widths were 550 ± 50 K for both $He(2^3S_1)$ and $Ar(4s^2[3/2]^o_2)$, and they were independent of the flow rates of N_2 and H_2. We assumed that the temperatures of $He(2^3S_1)$ and $Ar(4s^2[3/2]^o_2)$ represented the gas temperatures in the helium and argon-based plasmas, respectively.

3.6. Summary of diagnostics

Table 1 summarizes the comparison between the plasma parameters in the helium and argon-based plasmas. The most remarkable peculiarity is that the vibrational

temperature of molecular nitrogen in the helium plasma was higher than that in the argon-based plasma, even though the electron temperature was ultralow. To our knowledge, the vibrational temperature that is higher than the electron temperature is rare to observe. In addition, the densities of electronic excited states of molecular nitrogen and the density of atomic nitrogen were also higher in the ultralow-temperature helium plasma. We will discuss their mechanisms in the next section.

4. Discussion

4.1. Production processes of $N_2(B^3\Pi_g)$*,* $N_2(C^3\Pi_u)$*, and atomic nitrogen*

The higher N, $N_2(B^3\Pi_g)$, and $N_2(C^3\Pi_u)$ densities in the helium plasma are considered to be in connection with the higher vibrational temperature. As shown in Table 1, the $N_2(B^3\Pi_g)$ and $N_2(C^3\Pi_u)$ densities in the helium plasma were two orders of magnitude higher than those in the argon-based plasma. The production rates of $N_2(B^3\Pi_g)$ and $N_2(C^3\Pi_u)$ by electron impact excitation are proportional to the product of the electron density and the density of $N_2(X^1\Sigma_g^+)$. Even if we consider the fact that the central part of the helium plasma is an ionizing plasma which has a higher electron density than the argon-based plasma, the significantly higher densities of $N_2(B^3\Pi_g)$ and $N_2(C^3\Pi_u)$ in the helium plasma cannot be explained only by electron impact excitation. Figure 8 shows the rate coefficients of electron impact excitation for molecular nitrogen as a function of the electron temperature. The rate coefficients were calculated on the basis of the cross section data available in the LXCat database [50]. As shown in the figure, the rate coefficients for producing $N_2(B^3\Pi_g)$ and $N_2(C^3\Pi_u)$ by electron impact excitation of $N_2(X^1\Sigma_g^+)$ are steep functions of the electron temperature, and they are negligibly small at an electron temperature of 0.1 eV. Therefore, the production rates of $N_2(B^3\Pi_g)$ and $N_2(C^3\Pi_u)$ by electron impact excitation are negligible in the recombining plasma in the outside region. Another possible production process of $N_2(C^3\Pi_u)$ is the resonant energy transfer from argon metastable states to $N_2(X^1\Sigma_g^+)$. However, the rate of this reaction is negligible in comparison with electron impact excitation, since its rate coefficient is 4×10^{-20} m^3/s [51] and the $Ar(4s^2[3/2]_2^o)$ density ($< 3 \times 10^{15}$ m^{-3}) is lower than the electron density.

A possibility for the additional productions of $N_2(B^3\Pi_g)$ and $N_2(C^3\Pi_u)$ is the contribution of vibrational excited states. The productions of electronic excited states of molecular nitrogen have been observed in the spatial afterglow of nitrogen plasmas, and simulation works have pointed out the contribution of vibrational excited states [52–55]. Examples of the reaction processes are

$$N_2(X^1\Sigma_g^+, v \geq 39) + N \rightarrow N_2(A^3\Sigma_u^+) + N, \tag{2}$$

$$N_2(X^1\Sigma_g^+, 5 \leq v \leq 14) + N_2(A^3\Sigma_u^+) \rightarrow N_2(B^3\Pi_g) + N_2, \tag{3}$$

and

$$N_2(A^3\Sigma_u^+) + N_2(A^3\Sigma_u^+) \rightarrow N_2(C^3\Pi_u) + N_2. \tag{4}$$

The highly excited vibrational states, which are necessary in these reactions, are produced by the V-V (vibration-vibration) transition,

$$N_2(X^1\Sigma_g^+, v) + N_2(X^1\Sigma_g^+, w) \rightarrow N_2(X^1\Sigma_g^+, v+1) + N_2(X^1\Sigma_g^+, w-1). \quad (5)$$

Since the vibrational temperature of molecular nitrogen in the helium plasma is higher than that in the argon-based plasma, as shown in Table 1, it is possible to expect a higher rates for the V-V transition in the helium plasma. In addition, the production processes of atomic nitrogen via vibrational excited states

$$N_2(X^1\Sigma_g^+, 10 \leq v \leq 25) + N_2(X^1\Sigma_g^+, 10 \leq w \leq 25) \rightarrow N_2 + N + N \quad (6)$$

$$N_2(X^1\Sigma_g^+, 14 \leq v \leq 19) + N_2(A^3\Sigma_u^+) \rightarrow N_2 + N + N \quad (7)$$

may explain the higher N density in the helium plasma. Note that the assumption of the Boltzmann distribution in deducing the vibrational temperature from the threshold ionization curve does not contradict the importance of the V-V transition. The maximum shift of the threshold ionization curve shown in Fig. 6(a) is approximately 1 eV, corresponding to the detection of $N_2(X^1\Sigma_g^+, v = 3)$. The V-V transition distorts the population distribution at high vibrational quantum numbers, but the deviation from the Boltzmann distribution is not significant at $v \leq 3$ even if the V-V transition is active.

4.2. Mechanism for high vibrational temperature in helium plasma with ultralow electron temperature

The principal point to be discussed is the mechanism for the higher vibrational temperature in the helium plasma. The kinetics of vibrational excited states is basically governed by the e-V (electron-vibration), V-T (vibration-translation), and V-V transitions, and in addition to them, other chemical reactions participate in the kinetics. As shown in Fig. 8, the rate coefficient of electron impact vibrational excitation at an electron temperature of 1.7 eV is three orders of magnitude higher than that at 0.1 eV. Therefore, the argon-based plasma has the advantage in the e-V transition in comparison with the helium plasma. Since the gas temperatures are similar in the helium and argon-based plasmas, as shown in Table 1, the V-T transition does not result in the difference in the vibrational temperature. The rate of the V-V transition may be higher in the helium plasma because of the higher partial pressure of nitrogen. However, the V-V transition mainly affects the kinetics of highly excited vibrational states, and it may not explain the difference in the vibrational temperatures (or the population distribution at small v).

As mentioned above, the production processes of vibrational excited states in the helium plasma cannot be more efficient than those in the argon-based plasma. Hence, we have speculated that the destruction frequency of vibrational excited states is lower in the helium plasma. The electron impact excitation to electronic excited states can

work as a destruction process of $N_2(X^1\Sigma_g^+,v)$. For example, Fig. 9 shows the estimated rate coefficient of

$$N_2(X^1\Sigma_g^+, v) + e \rightarrow N_2(B^3\Pi_g) + e \tag{8}$$

as a function of the electron temperature. Since the cross section of this reaction is available only for $v = 0$, we assumed the same cross section for $N_2(X^1\Sigma_g^+,v)$ except the shift of the threshold energy when calculating Fig. 9. The magnitude of the shift was assumed to be equal to the vibrational energy. Since the rate coefficient increases with v, as shown in Fig. 9, reaction (8) may disturb the progress of the vibrational excitation or the increase in the vibrational temperature in the argon-based plasma with the electron temperature of 1.7 eV. In contrast, in the helium plasma with the ultralow electron temperature of 0.1 eV, the rate coefficient of reaction (8) is still negligible for higher vibrational states, resulting in the high vibrational temperature. We have proposed the same mechanism to explain more efficient CO_2 splitting via vibrational excited states in the plasma with an ultralow electron temperature [12].

5. Conclusions

In this paper, we reported the comparison between plasma parameters in a recombining helium plasma and an ionizing argon-based plasma. The major part of the helium plasma had an ultralow electron temperature of 0.1 eV, whereas the electron temperature of the argon-based plasma was 1.7 eV. We observed a higher vibrational temperature in the helium plasma (0.34 eV) than the argon-based plasma (0.18 eV). The higher vibrational temperature promoted the V-V transitions of molecular nitrogen, resulting in the higher densities of $N_2(B^3\Pi_g)$, $N_2(C^3\Pi_u)$, and atomic nitrogen. Since the rate coefficient of electron impact vibrational excitation is higher in the ionizing argon-based plasma, we have estimated that the destruction frequency of vibrational excited state is a key for the higher vibrational temperature in the helium plasma. The process we have proposed is electron impact excitation of $N_2(X^1\Sigma_g^+,v)$. The rate coefficient of this reaction is negligible even for vibrational excited states at the electron temperature of 0.1 eV, whereas it can work as a destruction process at 1.7 eV especially for highly excited vibrational states. It has been shown by the present work that a high-density plasma with a ultralow electron temperature is useful to obtain a high vibrational temperature and to promote reactions driven by vibrational excited states.

Acknowledgments

The authors are grateful to Kentaro Tomita and Toma Miyazawa for their help in laser Thomson scattering. This work was supported by JST CREST Grant No. JPMJCR19R3.

References

[1] Hong J, Prawer S and Murphy A B 2018 *ACS Sustainable Chem. Eng.* **6** 15
[2] Shah J, Wang W, Bogaerts A and Carreon M L 2018 *ACS Appl. Energy Mater.* **1** 4824
[3] Jauberteau J L, Jauberteau I and Aubreton J 2002 *J. Phys. D: Appl. Phys.* **35** 665
[4] Herzberg G 1970 *J. Mol. Spectro.* **33** 147
[5] Saikia P and Kakati B 2013 *J. Vac. Sci. Technol. A* **31** 061307
[6] Itagaki N, Iwata S, Muta K, Yonesu A, Kawakami S, Ishii N and Kawai Y 2003 *Thin Solid Films* **435** 259
[7] Sasaki K, Kokubu H, Hayashi D and Kadota K 2001 *Thin Solid Films* **386** 243
[8] Abrar M, Qayyum A, Gilani A R, Khan A W, Saeed A, Naseer S and Zakaullah M 2013 *Curr. Appl. Phys.* **13** 969
[9] Peterson J R, Padellec A L and Danared H 1998 *J. Chem. Phys.* **108** 1978
[10] Brian J and Mitchell A 1990 *Phys. Rep.* **186** 215
[11] Whitaker M, Biondi M A and Johnsen R 1981 *Phys. Rev. A* **24** 743
[12] Yamazaki M, Nishiyama S and Sasaki K 2020 *Plasma Sources Sci. Technol.* **29** 115016
[13] Kozák T and Bogaerts A 2014 *Plasma Sources Sci. Technol.* **23** 045004
[14] Aerts R, Martens T and Bogaerts A 2012 *J. Phys. Chem. C* **116** 23257
[15] Liu S, Winter L R and Chen J G 2020 *ACS Catal.* **10** 2855
[16] Li D, Rohani V, Fabry F, Ramaswamy A P, Sennour M and Fulcheri L 2020 *Appl. Catal. B: Environ.* **261** 118228
[17] Juurlink L B F, McCabe P R, Smith R R, DiCologero C L and Utz A L 1999 *Phys. Rev. Lett.* **83** 868
[18] Rettner C T, Auerbach D J and Michelsen H A 1992 *Phys. Rev. Lett.* **68** 1164
[19] Rouwenhorst K H R and Lefferts L 2021 *J. Phys. D: Appl. Phys.* **54** 393002
[20] Miyazaki E 1980 *J. Catal.* **65** 84
[21] Zhao C and Wu H 2018 *Appl. Surf. Sci.* **435** 1199
[22] Quan J, Muttaqien F, Kondo T, Kozarashi T, Mogi T, Imabayashi T, Hamamoto Y, Inagaki K, Hamada I, Morikaww Y, and Nakamura J 2019 *Nat. Chem.* **11** 722
[23] Winters C, Hung Y C, Jans E, Eckert Z, Frederickson K, Adamovich I V and Popov N 2017 *J. Phys. D: Appl. Phys.* **50** 505203
[24] Klarenaar B L M, Engeln R, van den Bekerom D C M, van de Sanden M C M, Morillo-Candas A S and Guaitella O 2017 *Plasma Sources Sci. Technol* **26** 115008
[25] Silva T, Grofulović M, Klarenaar B L M, Morillo-Candas A S, Guaitella O, Engeln R, Pintassilgo C D and Guerra V 2018 *Plasma Sources Sci. Technol* **27** 015019
[26] Damen M A, Martini L M and Engeln R 2020 *Plasma Sources Sci. Technol* **29** 065016
[27] van den Bekerom D C M, van de Steeg A, van de Sanden M C M and van Rooij G J 2020 *J. Phys. D: Appl. Phys.* **53** 054002
[28] Kuhfeld J, Lepikhin N D, Luggenhölscher D and Czarnetzki U 2021 *J. Phys. D: Appl. Phys.* **54** 305204
[29] Du Y, Tsankov T V, Luggenhölscher D and Czarnetzki U 2021 *J. Phys. D: Appl. Phys.* **54** 365201
[30] Richards C, Jans E, Gulko I, Orr K and Adamovich I V 2022 *Plasma Sources Sci. Technol* **31** 034001
[31] Rehman N U, Khan F U, Khattak N A D and Zakaullah M 2008 *Phys. Lett. A* **372** 1462
[32] Koike S, Sakamoto T, Kobori H, Matsuura H and Akatsuka H 2004 *Jpn. J. Appl. Phys.* **43** 5550
[33] Hong Y, Lu N, Pan J, Li J, Wu Y and Shang K 2013 *IEEE Trans. Plasma Sci.* **41** 545
[34] Aramaki M, Kato K, Goto M, Muto S, Morita S and Sasaki K 2004 *Jpn. J. Appl. Phys.* **43** 1164
[35] van Gessel A F H, Carbone E A D, Bruggeman P J and van der Mullen J J A M 2012 *Plasma Sources Sci. Technol.* **21** 015003
[36] Bischel W K and Black G 1983 *AIP Conference Proceedings* **100** 181
[37] Ohno N, Tanaka N, Ezumi N, Nishijima D and Takamura S 2001 *Contrib. Plasma Phys.* **41** 473

[38] Hayashi Y, Nishikata H, Ohno N, Kajita S, Tanaka H, Oshima H and Seki M 2019 *Contrib. Plasma Phys.* **59** e201800088
[39] Glimore F R, Laher R R and Espy P J 1992 *J. Phys. Chem. Ref. Data* **21** 1005
[40] Loureiro J and Ferreira C M 1986 *J. Phys. D* **19** 17
[41] Hosoyama S, Yamazaki M and Sasaki K 2022 *Plasma Fusion Res.* **17** 1406070
[42] Black G, Wise H, Schechter S and Sharpless R L 1974 *J. Chem. Phys.* **60** 3526
[43] Fujimoto T, Iwamae A and Goto M 2007 chap.2
[44] Fujimoto T 1979 *J. Phys. Soc. Jpn.* **47** 273
[45] Fujimoto T 1980 *J. Phys. Soc. Jpn.* **49** 1569
[46] Shibagaki K and Sasaki K 2008 *J. Phys. D: Appl. Phys.* **41** 195204
[47] Nishijima D, Wenzel U, Motoyama M, Ohno N, Takamura S and Krasheninnikov S I 2001 *J. Nucl. Mater.* **290-293** 688
[48] Hinnov E and Hirschberg J G 1962 *Phys. Rev.* **125** 795
[49] Hahn Y 2000 *Phys. Lett. A* **264** 465
[50] Cartwright D C, Chutjian A, Trajmar S and Williams W 1977 *Phys. Rev. A* **16** 1013
[51] Greig A, Charles C and Boswell R W 2016 *Phys. Plasmas* **23** 013508
[52] Sadeghi N, Foissac C and Supiot P 2001 *J. Phys. D: Appl. Phys.* **34** 1779
[53] Guerra V, Sá P A and Loureiro J 2007 *J. Phys. Conf. Ser.* **63** 012007
[54] Horikawa Y, Hayashi T and Sasaki K 2013 *J. Phys. Conf. Ser.* **441** 012009
[55] Guerra V, Sá P A and Loureiro J 2004 *Eur.Phys. J. Appl. Phys.* **28** 125

Table 1. Comparison of the helium and argon-based plasmas used in the present experiment. $[N_2(X^1\Sigma_g^+)]$ shows the densities of molecular nitrogen before producing the plasmas.

Parameters	Units	Helium plasma	Argon-based plasma
$[N_2(X^1\Sigma_g^+)]$	m^{-3}	9.7×10^{19}	1.6×10^{19}
T_e	eV	0.10 ± 0.02	1.7 ± 0.2
n_e	m^{-3}	$(6.0 \pm 0.6) \times 10^{18}$	$(8.0 \pm 0.8) \times 10^{17}$
$[N_2(B^3\Pi_g)]$	m^{-3}	$(5.0 \pm 0.1) \times 10^{14}$	$(7 \pm 2) \times 10^{12}$
$[N_2(C^3\Pi_u)]$	m^{-3}	$(1.0 \pm 0.1) \times 10^{13}$	$(1.0 \pm 0.1) \times 10^{11}$
[N]	m^{-3}	$(2.0 \pm 0.2) \times 10^{19}$	$< 2 \times 10^{18}$
$T_v(N_2)$	eV	0.34 ± 0.04	0.18 ± 0.04
T_g	K	550 ± 50	550 ± 50

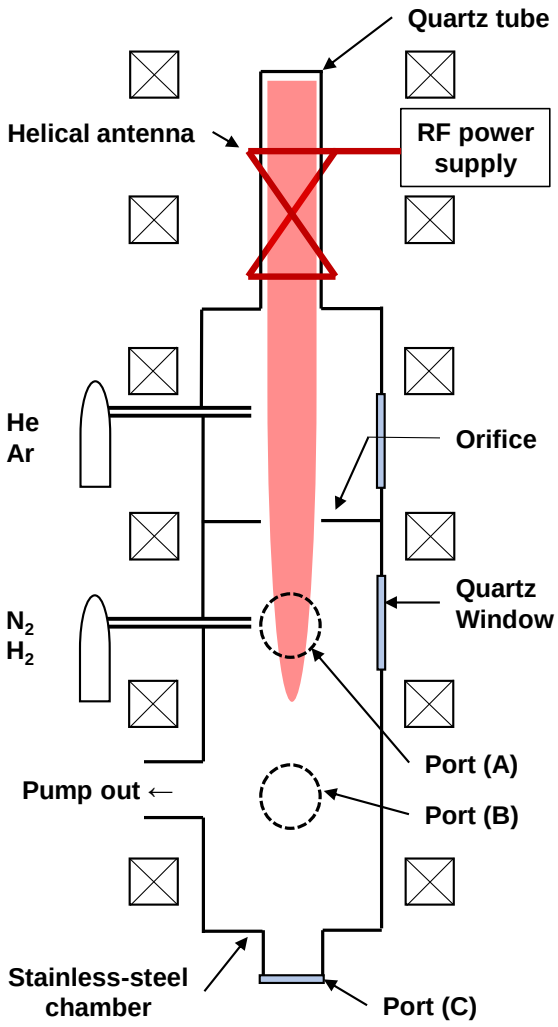

Figure 1. Plasma source and arrangement of observation ports.

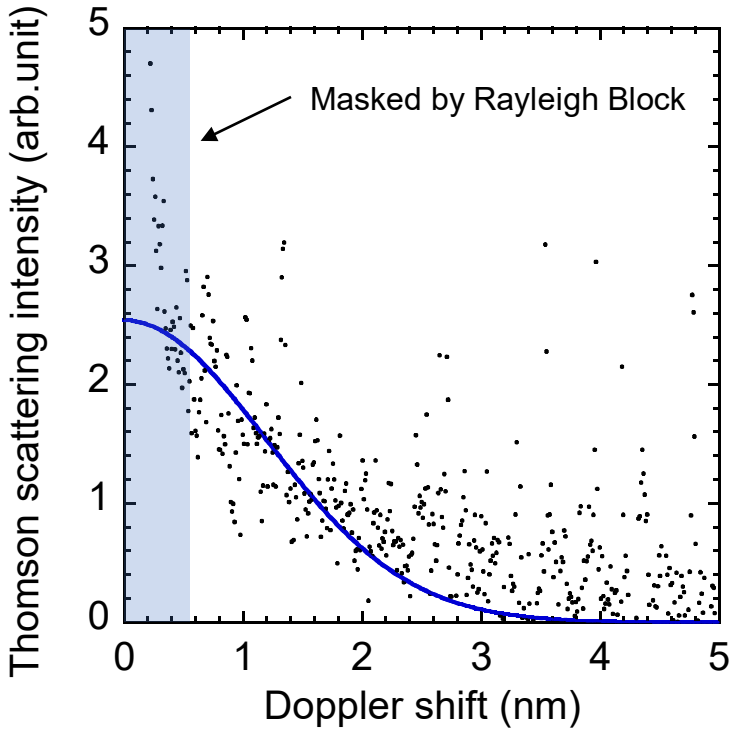

Figure 2. Thomson scattering spectrum observed on the cylindrical axis of the helium plasma.

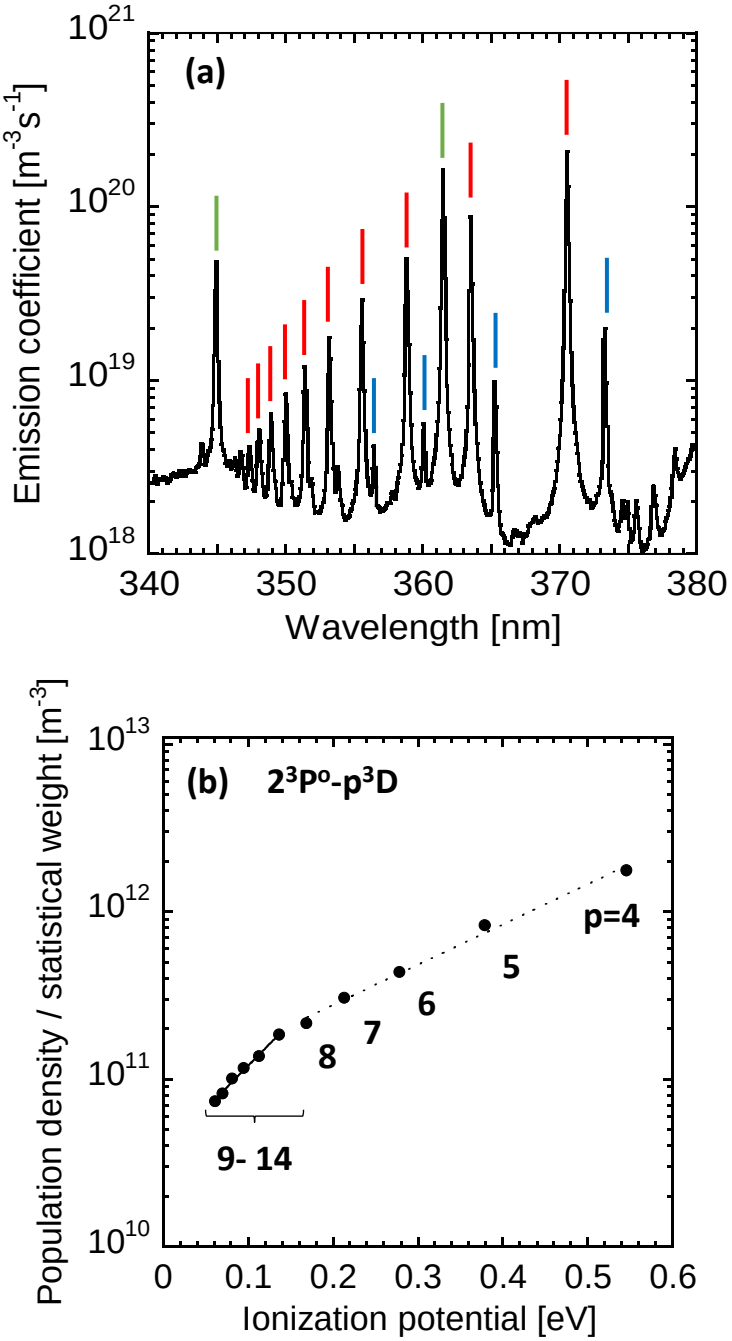

Figure 3. a) Optical emission spectrum of the helium plasma. This spectrum was observed in the upstream-chamber just above the orifice. The red, green, and blue bars indicate that the optical emission lines are assigned to the transitions of $2^3\mathrm{P^o} - p^3\mathrm{D}$ ($p = 7 - 16$), $2^1\mathrm{S} - p^1\mathrm{P^o}$ ($p = 5, 6$), and $2^3\mathrm{P^o} - p^3\mathrm{S}$ ($p = 7 - 10$), respectively. (b) Relationship between the population density of He(p^3D) and the ionization potential.

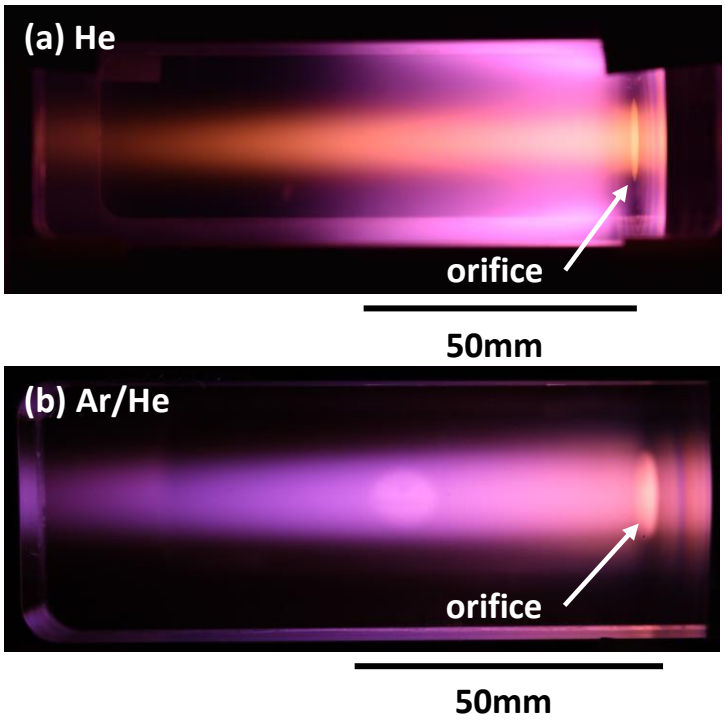

Figure 4. Photographs of (a) the helium and (b) argon-based plasmas.

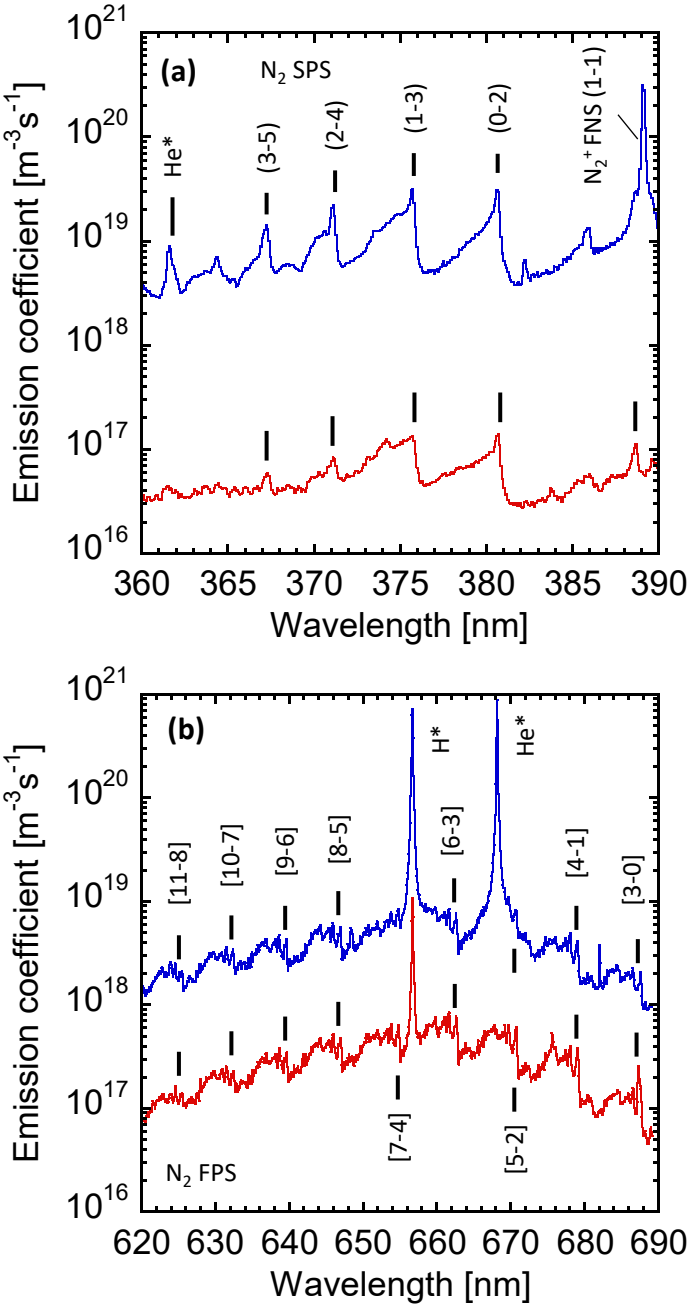

Figure 5. Optical emission spectra of the helium and argon-based plasmas in the wavelength ranges of (a) the second and (b) first positive systems of molecular nitrogen.

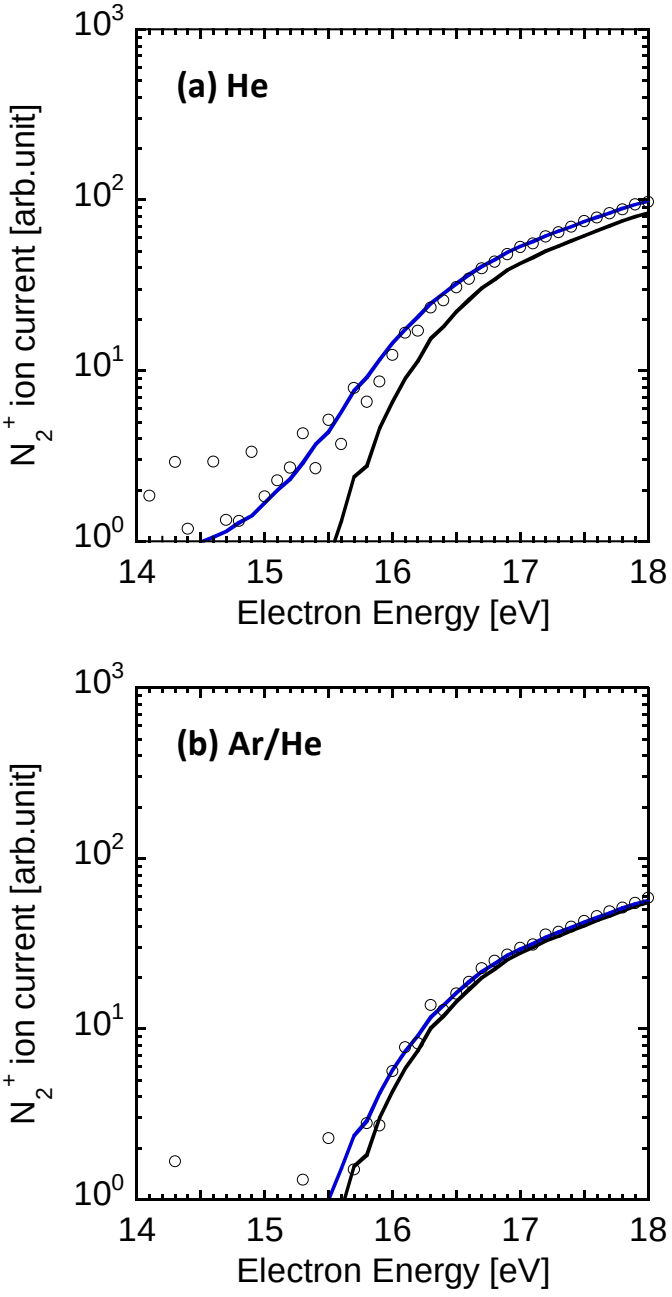

Figure 6. Threshold ionization curves at $m/z = 28$ observed in the (a) helium and (b) argon-based plasmas.

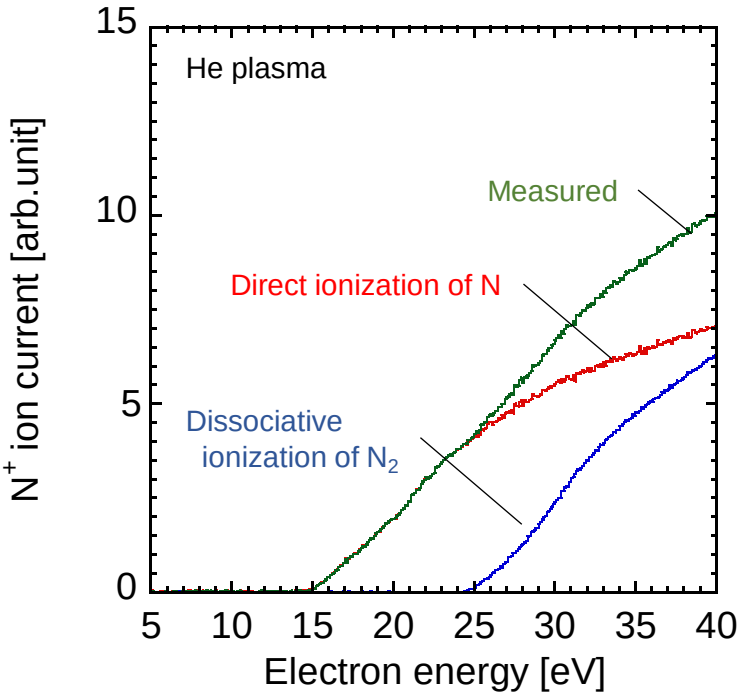

Figure 7. Threshold ionization curve at $m/z = 14$ observed in the helium plasma.

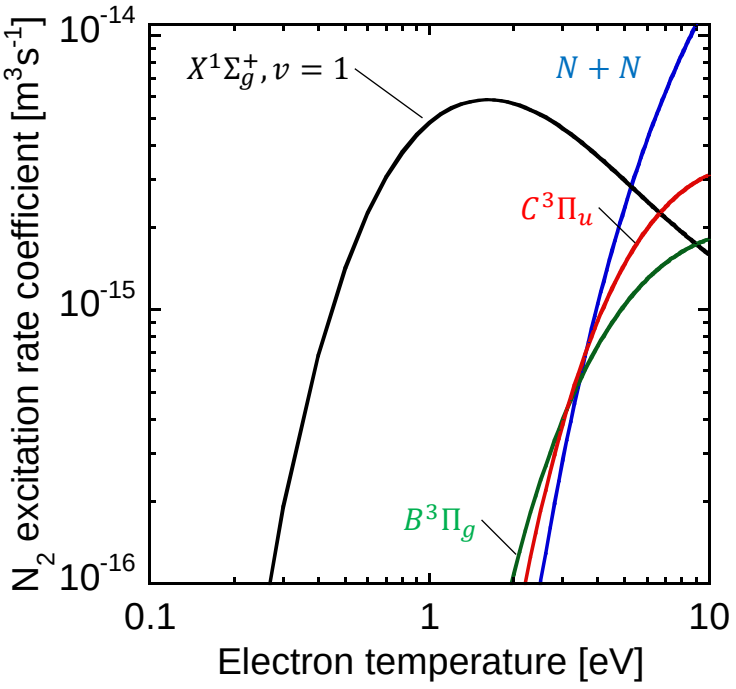

Figure 8. Rate coefficients of electron impact excitation for molecular nitrogen as a function of the electron temperature.

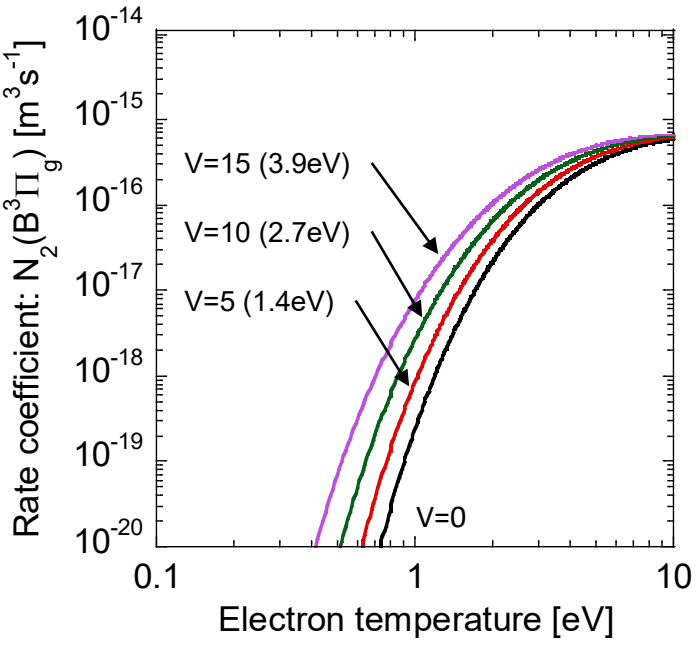

Figure 9. Estimated rate coefficient of $N_2(X^1\Sigma_g^+, v) + e \rightarrow N_2(B^3\Pi_g) + e$ as a function of the electron temperature.